Immobilization of Pt Nanoparticles via Rapid and Reusable Electropolymerization of Dopamine on TiO_2 Nanotube Arrays for Reversible SERS Substrates and Nonenzymatic Glucose Sensors

Jingsheng Cai, Jianying Huang, Mingzheng Ge, James Iocozzia, Zhiqun Lin, Ke-Qin Zhang, and Yuekun Lai**

Inspired by mussel-adhesion phenomena in nature, polydopamine (PDA) coatings are a promising route to multifunctional platforms for decorating various materials. The typical self-polymerization process of dopamine is time-consuming and the coatings of PDA are not reusable. Herein, a reusable and time-saving strategy for the electrochemical polymerization of dopamine (EPD) is reported. The PDA layer is deposited on vertically aligned TiO_2 nanotube arrays (NTAs). Owing to the abundant catechol and amine groups in the PDA layer, uniform Pt nanoparticles (NPs) are deposited onto the TiO_2 NTAs and can effectively prevent the recombination of electron–hole pairs generated from photo-electrocatalysis and transfer the captured electrons to participate in the photo-electrocatalytic reaction process. Compared with pristine TiO_2 NTAs, the as-prepared Pt@TiO_2 NTA composites exhibit surface-enhanced Raman scattering sensitivity for detecting rhodamine 6G and display excellent UV-assisted self-cleaning ability, and also show promise as a nonenzymatic glucose biosensor. Furthermore, the mussel-inspired electropolymerization strategy and the fast EPD-reduced nanoparticle decorating process presented herein can be readily extended to various functional substrates, such as conductive glass, metallic oxides, and semiconductors. It is the adaptation of the established PDA system for a selective, robust, and generalizable sensing system that is the emphasis of this work.

J. S. Cai, Prof. J. Y. Huang, M. Z. Ge,
Prof. K.-Q. Zhang, Prof. Y. K. Lai
National Engineering Laboratory for Modern Silk
College of Textile and Clothing Engineering
Soochow University
Suzhou 215123, P. R. China
E-mail: yklai@suda.edu.cn

J. Iocozzia, Prof. Z. Q. Lin
School of Materials Science and Engineering
Georgia Institute of Technology
Atlanta, GA 30332, USA
E-mail: zhiqun.lin@mse.gatech.edu

DOI: 10.1002/smll.201604240

1. Introduction

Nanostructured titanium dioxide (TiO_2) materials have attracted increased attention due to their relatively high conductivity, low cost, environmental safety, corrosion resistance, and mechanical stability.[1–5] As a novel semiconductor material, TiO_2 finds applications in photo-electrocatalytic degradation of organic pollutants, gas sensors, dye-sensitized solar cells, and electrocatalysis water splitting.[6–10] However, due to the recombination of photogenerated electron–hole pairs, a wide band gap (3.2 eV for anatase, 3.0 eV for rutile), and a low quantum efficiency for photocatalytic activity, TiO_2 can only absorb UV light which accounts for less than 5%

over the entire solar spectrum.[11] Owing to their large aspect ratio, nontoxicity, excellent electron-transfer behavior, and a large number of active sites for chemical reactions, TiO_2 nanotubes have been employed in bioelectrochemical applications including in catalyst loading for glucose electrocatalytic oxidation.[12]

Dopamine (3,4-dihydroxyphenylethylamine), an important hormone and neurotransmitter present in most animals, plays an important role in mammals as a chemical messenger.[13] Inspired by the composition of bioadhesive proteins in marine mussels, dopamine was found to be able to mimic the specialized adhesive foot protein, Mefp-5 (Mytilus edulis foot protein-5), which is secreted by mussels and spontaneously polymerizes n weakly alkaline aqueous medium under ambient conditions to form a polydopamine (PDA) coating.[14] The resultant PDA has attracted great interest as a biomimetic polymer that has been widely exploited for antifouling,[15] self-healing hydrogels,[16] antibacterials,[17] dye removal,[18] and lithium-ion-battery separators.[19] Possessing catechol, phenolic, and amine functional groups,[20] PDA-functionalized surfaces provide a versatile platform that can grow and tightly adhere to almost all organic and inorganic substrates, such as noble metals, metal oxides, semiconductors, ceramics, and synthetic polymers.[21] These surface functional groups endow the PDA surface with the ability for anchoring and growing different metal NPs (Ag, Pt, Au) via an in situ reduction process onto various substrates.[22] Additionally, PDA is both an environmentally friendly and biocompatible material enabling its use in living systems. Thus, PDA offers a mild and green approach to anchor NPs into various substrates without the need for toxic reagents or expensive catalysts. To date, this system has been successfully applied in various areas.[23]

Recently, Raman spectroscopy has been used for characterization of a set of nanomaterials including carbon nanotubes, titania, graphene, and so on.[24] However, a disadvantage is its relatively weak Raman signal from molecules. Surface enhanced Raman scattering (SERS) is a label-free and highly sensitive analytical tool to molecular fingerprint on the basis of electromagnetic mechanism (EM) and chemical mechanism (CM) of SERS.[25] The EM enhancement can be realized by the surface plasmons excited between noble metal particles under visible irradiation.[26] On the other hand, the CM enhancement is introduced through three mechanisms, namely, charge transfer between SERS substrate and probe molecule, molecule resonance, and interfacial nonresonant interactions.[27] To date, various noble metal SERS substrates, such as Au, Ag, Cu, and their combinations, have been employed to achieve highly enhanced SERS effect. However, the study of Pt substrate for SERS has been rarely reported.

With the emergence of diabetes mellitus as an international public health problem, quick and effective estimation and monitoring of glucose is of importance in various fields such as biotechnology, blood sugar analysis, and food industry.[28] Numerous efforts have been devoted to construct different types of glucose sensors since Clark and Lyons utilized glucose oxidases to exploit the first enzyme electrode more than 50 years ago.[29] Several earlier reports regarding the enzymatic estimation of glucose are available.[30] However, they are limited by their instability, complex enzyme immobilization, and high sensitivity to temperature, pH, and humidity.[31] To circumvent these drawbacks, nonenzymatic sensors, based on noble metal nanoparticles (such as Au, Pd, and Pt) or metal oxides (such as NiO, CuO, and Co_3O_4),[32] have garnered much attention as alternatives for sensing. This is because nanocomposites combining diverse kinds of nanomaterials can greatly boost the catalytic activity of glucose sensors. Herein, we report a facile strategy for creating biosensors utilizing PDA to induce the reduction of Pt nanoparticles (NPs) on TiO_2 nanotube arrays (NTAs). Apart from the advantages noted above, the as-prepared electrodes are also minimally affected by the presence of other biomolecules such as uric acid (UA) and ascorbic acid (AA),[33] while maintaining the long-term stability and self-cleaning attributes.

The self-polymerization of dopamine in an aqueous weakly alkaline condition in the presence of dissolved oxygen has been shown to be an effective way to quickly coat PDA films onto various substrates.[34] However, several obstacles still face this method. First, the typical reaction needs to be performed in an alkaline environment. Thus, alkaline-sensitive materials cannot be modified directly. Second, the low PDA deposition rate requires a reaction time ranging from hours to days and the PDA solution cannot be reused. Moreover, the reaction is limited to continuous stirring and oxygen-containing environments. To address these limitations, a variety of methods were employed including UV irradiation, oxidant promotion, and electrochemical actuation.[35] A strategy to speed up the polymerization by utilizing $CuSO_4/H_2O_2$ as a trigger has recently been reported.[36] However, the extra Cu^{2+} may become incorporated into the PDA layer to some extent as a possible contaminant. The electropolymerization of dopamine to immobilize bioactive molecules for surface functionalization in cardiovascular stents was also studied.[37] Notably, these strategies have seen limited use in practical applications due to the requirement of toxic reagents/catalyst, poor reutilization, long reaction time, and a lack of uniform films.

Herein, we developed a fast, reusable strategy for the electrochemical-induced polymerization of dopamine (EPD) under mild acid conditions to deposit PDA films onto TiO_2 NTAs. Subsequent metal adsorption and reduction on the surface of the composites was also presented. This EPD strategy offers a fast and cost-effective process to construct PDA films on TiO_2 NTAs in minutes. The electropolymerization process of dopamine on TiO_2 NTAs is ten times faster than that of the previous works.[37] More importantly, the dopamine-containing electrolyte can be reused to coat samples with uniform PDA film more than ten times (20 cycles of cyclic voltammetry (CV) technique each time), representing a marked improvement of recycling ability. By taking advantage of the strong reducing ability of PDA, we successfully anchored Pt, Au, and Pd NPs onto TiO_2 NTAs to yield a uniform M@TiO_2 NTA (M = Pt, Au, and Pd). When compared with pristine TiO_2 NTAs, the as-prepared Pt@TiO_2 NTA composites exhibited enhanced photocurrent densities. Furthermore, the Pt@TiO_2 NTAs can act as recyclable and

UV-assisted self-cleaning substrates for SERS measurements and the detection of tracing rhodamine 6G (R6G). It is notable that the electrocatalytic ability of Pt@TiO_2 NTA electrodes toward glucose oxidation was explored for nonenzymatic blood glucose detection.

2. Result and Discussion

2.1. Fabrication and Characterization of PDA-Modified TiO_2 NTAs

Multiple scanning cyclic voltammetry was chosen for EPD. **Figure 1**a shows the typical CV curves of dopamine (2 mg mL^{-1}) in 1 mg mL^{-1} Tris buffer (adjusted by HCl to pH = 7.4) polymerized on the TiO_2 NTAs at a scan rate of 0.2 V s^{-1} with the potential ranging from –1.0 to 1.0 V for 20 cycles in the first process. In each cycle, one clear broad anodic peak and one smaller cathodic peak appeared at around –0.3 V and the observed responses could be attributed to the coupled intermediate products dopamine/dopaminequinone and leucodopaminechrome/dopaminechrome. All peak point currents decreased slightly with the increase of potential scans apart from the first cycle. After 20 cycles, PDA had been deposited onto the TiO_2 NTAs, which then acted as the working electrodes. Figure 1b displays the CV measurements on TiO_2 NTAs during the EPD of the tenth process. Similar characteristic peak positions and current values are observed, suggesting that the dopamine-containing electrolyte can be reused for multiple electropolymerization processes. Figure 1e describes the proposed mechanism for the electropolymerization of dopamine. The polymerization begins with the oxidation of the catechol moiety to a quinone with the subsequent cyclization into leucodopaminechrome. After rearrangement, the intermediate product (5,6-dihydroxyindole) polymerizes through deprotonation and intermolecular Michael addition

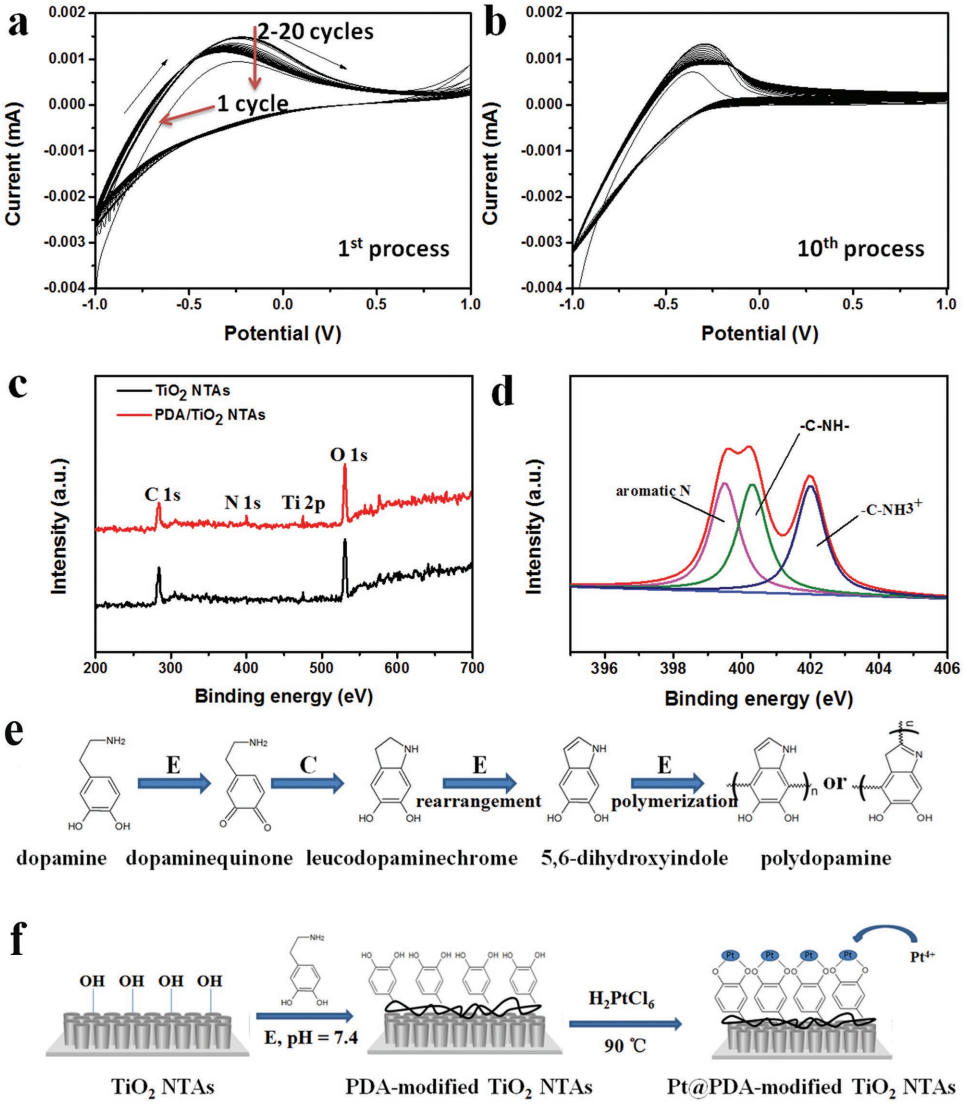

Figure 1. a) Cyclovoltammetry measurements on TiO_2 NTAs during EPD. b) Cyclovoltammetry measurements on TiO_2 NTAs during EPD after ten process cycles. c) XPS spectra of TiO_2 NTAs and PDA-modified TiO_2 NTAs. d) N 1s high-resolution spectra of PDA-modified TiO_2 NTAs. e) Mechanism for EPD. "E" denotes electrochemical reactions and "C" denotes chemical reactions. f) Illustration of the procedure for preparing Pt@TiO_2 NTAs.

to yield a cross-linked homopolymer. The formed PDA films act as the functional platform upon which the adsorption of Pt ions and subsequent Pt NP immobilization can readily occur. The preparation of Pt NPs on PDA-modified TiO_2 NTAs is schematically illustrated in Figure 1f. The X-ray photoelectron spectrometer (XPS) spectra of PDA-modified TiO_2 NTAs clearly show the presence of the N 1s peak which is absent in the pristine TiO_2 NTAs (Figure 1c). The amine groups (−C−NH) are present at 400.3 eV as well as protonated N ($C-NH^{3+}$) at 402.0 eV and aromatic N at 399.5 eV obtained from deconvolution analysis (Figure 1d).[38] These results confirm the formation of PDA on the TiO_2 NTAs.[39] The PDA coatings on the surface of the TiO_2 NTAs were further verified by performing energy-dispersive X-ray spectroscopy (EDX) of an area of PDA-modified TiO_2 NTAs (Figure S1, Supporting Information). No nitrogen signal was observed in the pristine TiO_2 NTAs as seen in Figure S1a (Supporting Information). In PDA-modified TiO_2 NTAs, nitrogen emerged and occupied an atomic percentage of 0.75% (Figure S1b, Supporting Information). The mapping of N demonstrated an evenly distributed dot pattern, indicating the PDA film was uniformly coated on the surface of the TiO_2 NTAs.

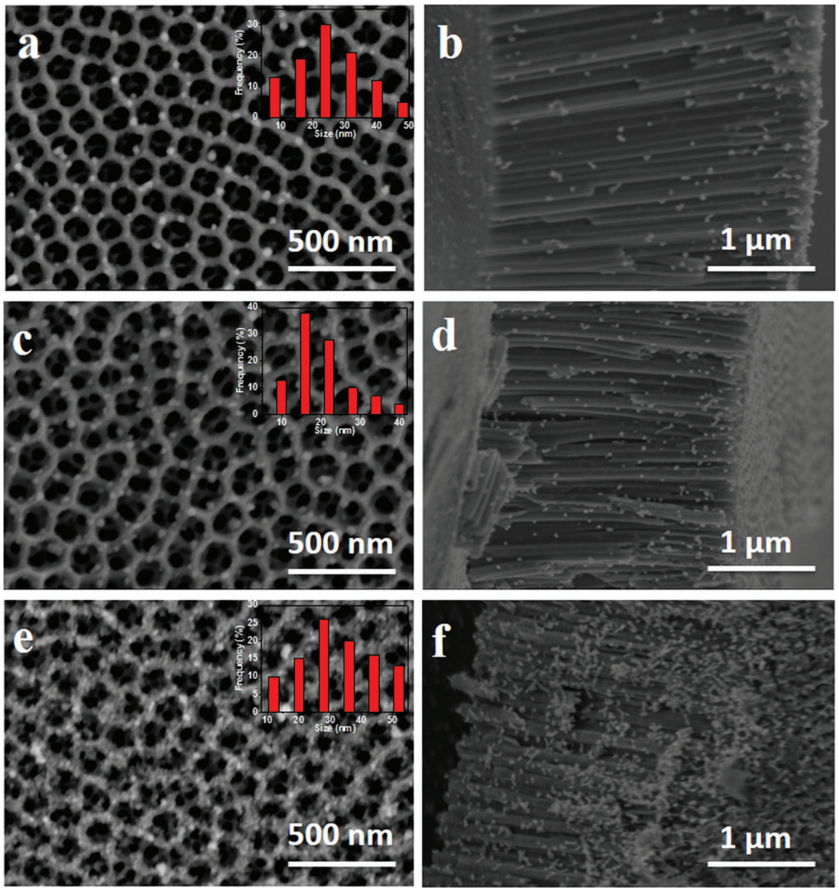

Figure 2. a,c,e) Typical top-view and b,d,f) side-view scanning electron microscopy (SEM) images of Pt@TiO_2 NTAs with different concentrations (0.1×10^{-3}, 0.2×10^{-3}, 0.4×10^{-3} M, respectively) of Pt^{4+} ions by in situ reduction reaction under 90 °C for 3 h after PDA modification. Insets of (a), (c), (e) are the size distributions of Pt NPs on the TiO_2 NTAs.

2.2. Characterization of EPD-Reduced Pt@TiO_2 NTAs

Figure 2 compares the top and side views of Pt@TiO_2 NTAs with different concentrations (0.1×10^{-3}, 0.2×10^{-3}, 0.4×10^{-3} M, respectively) of Pt^{4+} ions subsequently reduced at 90 °C for 3 h after PDA modification. Small Pt NPs anchored on the surface of aligned TiO_2 NTAs formed when immersed in 50 mL of 0.1×10^{-3} M chloroplatinic acid solution (Pt precursor) with an average size of 15–25 nm (Figure 2a). With the increase of Pt^{4+} ion concentration, the amount of uniformly distributed Pt NPs is increased on TiO_2 NTAs, while the size of the Pt NPs remained constant. With a further increase in the concentration of the Pt^{4+} ions to 0.2×10^{-3} M, the number density of Pt NPs on the TiO_2 NTAs increased threefold (Figure 2c). At the Pt^{4+} ion concentration of 0.4×10^{-3} M, clusters of Pt NPs aggregated at the entrances of TiO_2 NTAs without blocking them. Figure 2e shows that the formed Pt nanoparticles with an average diameter of about 30 nm are compactly scattered at the surface of TiO_2 NTA substrate. The aggregation shapes of Pt nanoparticles can greatly enhance the active surface area of the substrate. At 0.8×10^{-3} M, Pt NPs aggregated and nearly blocked the entrances of the TiO_2 NTAs (Figure S2, Supporting Information). In addition to the concentration of chloroplatinic acid solution, parameters such as the temperature, reduction time, and the CV cycles were also varied (Figures S3–S5, Supporting Information). It is clear that the TiO_2 NTAs modified by PDA retain the highly ordered tubular structures. The amount and morphology of the Pt NPs can be easily controlled by adjusting these parameters. Moreover, this facile green EPD-induced reduction strategy can be extended to successfully fabricate Au@TiO_2 NTAs and Pd@TiO_2 NTAs with uniform particle size and narrow size distribution. A detailed description can be found in Figures S6–S8 (Supporting Information).

The composition and configuration of Pt@TiO_2 NTAs modified by PDA were estimated by XPS. The corresponding spectra are shown in **Figure 3**a,b. Binding energy peaks for C 1s (284.5 eV), O 1s (532.4 eV), and Ti 2p (458.9 eV) can be seen in both pristine TiO_2 NTAs and EPD-reduced Pt@TiO_2 NTAs in Figure 3a. In addition, the spectrum of Pt@TiO_2 NTAs shows the Pt 4f peak. The high resolution XPS spectra of the Pt 4f region are shown in Figure 3b. The spectrum of Pt 4f was fitted to two distinct peaks (Pt $4f_{7/2}$ and Pt $4f_{5/2}$) with a wide gap of 3.4 eV. These observations indicate that Pt mainly exists in the Pt^0 state on the surface of the TiO_2 NTAs.[40]

X-ray diffraction (XRD) patterns of EPD-reduced Pt@TiO_2 NTAs and the corresponding references are shown

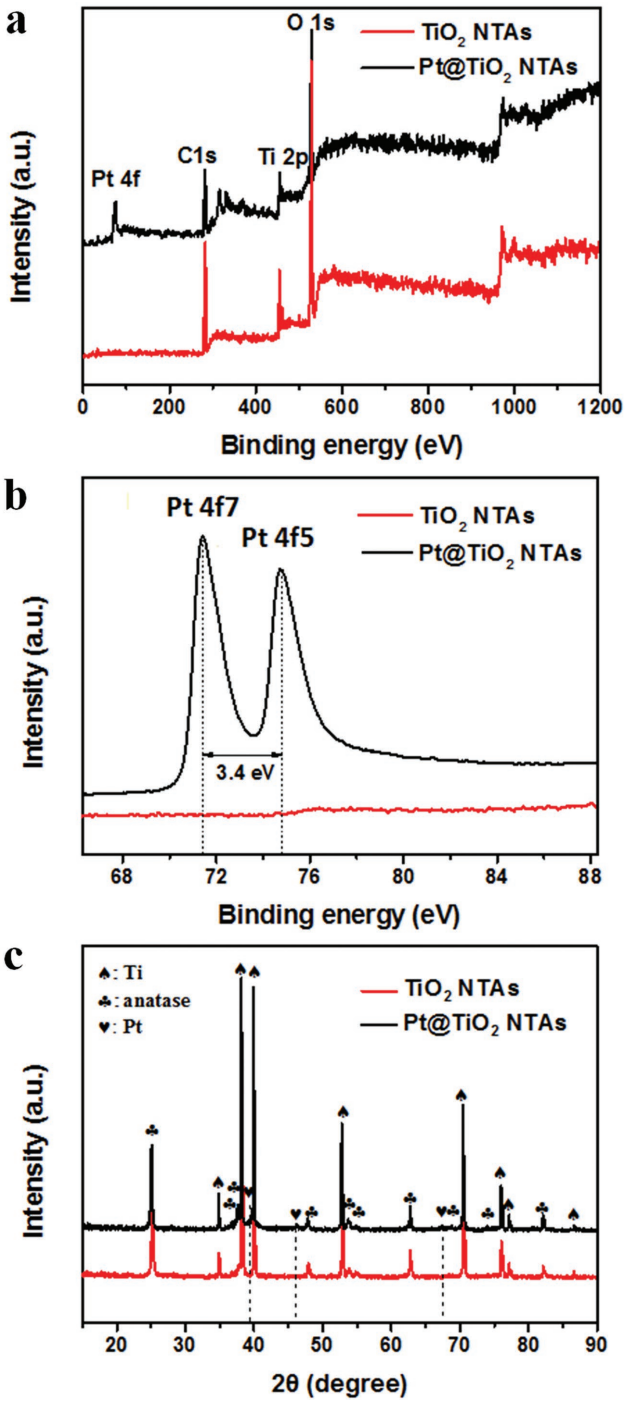

Figure 3. a) XPS spectrum and b) high resolution XPS spectra of pristine TiO_2 and EPD-reduced Pt@TiO_2 NTAs using 0.4×10^{-3} M chloroplatinic acid solution. c) XRD patterns of pure TiO_2 NTAs and EPD-reduced Pt@TiO_2 NTAs using 0.4×10^{-3} M chloroplatinic acid solution.

in Figure 3c. For bare TiO_2 NTAs, the diffraction peaks at 25.3°, 37.9°, 48.0°, and 53.9° could be well indexed to the (101), (004), (200) and (105) planes of the TiO_2 anatase phase, respectively (JCPDS no. 21-1272). After PDA-induced reductive reaction to form Pt NPs, three additional peaks appeared at 39.8°, 46.2°, and 67.4°, in agreement with the standard diffraction peaks of Pt (JCPDS no. 04-0802) corresponding to the (111), (200) and (220) planes of Pt, respectively. The results qualitatively agree with transmission electron microscope (TEM) measurements as well. However, the Pt (111) peak shows a weak intensity as it might be masked by the peak at 40.1° of Ti substrate whose signal is more dominant. The diffraction peaks of the (200) and (220) planes of Pt cannot be distinctly observed compared with the other planes. This is likely a result of the small size of the Pt NPs or the high dispersion of Pt NPs on the TiO_2 NTAs.[41]

TEM measurement revealed the growth of numerous uniform Pt NPs adhered tightly to the PDA films on the TiO_2 NTAs due to the reduction ability and metal-binding affinity of the catechol groups of PDA (**Figure 4**a,b). High resolution transmission electron microscope (HRTEM) image (Figure 4c) and selected area electron diffraction (SAED) of the area (Figure 4b) support the presence of two types of resolved lattice fringes of 0.227 and 0.352 nm, corresponding to the *d*-spacing of the (101) plane of anatase TiO_2 and the (111) plant of Pt, respectively.[42] The electron diffraction pattern of Pt@TiO_2 NTAs shows discontinuous, diffraction rings, indicating the presence of grains of the hydride phases during the formation process of the Pt NPs. The results above are consistent with the analysis of the XRD patterns. EDX and element mapping (Figure 4d,e) were used to further verify the presence and distribution of the main elements of several EPD-reduced Pt@TiO_2 NTAs. The Pt NPs occupy roughly 2.16% of the atomic percentage and are uniformly anchored on the TiO_2 NTAs comparable to the uniform distribution of Ti and O from the TiO_2 NTAs.

UV–vis diffuse reflection spectroscopy (UV-DRS) enable the measurement of the visible-light photocatalytic character of pristine TiO_2 NTAs and TiO_2 NTAs with different amounts of Pt NPs (**Figure 5**a). Bare TiO_2 NTAs exhibited a good absorption band in the 380 nm region which contributes to the charge transfer from the O 2p valence band to the Ti 3d conduction band. Compared to pristine TiO_2 NTAs, EPD-reduced Pt@TiO_2 NTAs enhance the photoconversion quantum yield, and the absorption values of EPD-reduced Pt@TiO_2 NTAs initially increased with the increasing precursor concentration to achieve a maximum relative absorption intensity for Pt@TiO_2 NTA-0.4. Further increasing the precursor concentration led to a relative absorption intensity decrease in the composite electrode (Pt@TiO_2 NTA-0.8). In particular, plasmonic coupling can be used to generate localized surface plasmon resonances in transition metal dimeric nanoantennas over a broad spectral range (from visible to near infrared) and that the position of the resonance can be controlled through morphological variation of the Pt NPs (size, shape, and interparticle distance).[43] It is known that greater relative absorption intensity in visible region renders better photocatalytic activity. As shown in Figure 5a, the sample of Pt@TiO_2 NTA-0.4 possessed the best relative adsorption value in the visible spectrum and consequently displayed the best photocurrent response.

The separation of photogenerated electron–hole pairs was evaluated by measuring the photocurrent responses. Figure 5b explains the transient photocurrent responses of pristine TiO_2 NTAs and Pt@TiO_2 NTA-0.4 used as the photoelectrodes in the dark and under visible light in 0.1 M Na_2SO_4 by chronoamperometry. Whether with or without Pt NPs, the photocurrent density increased when the light was on, and

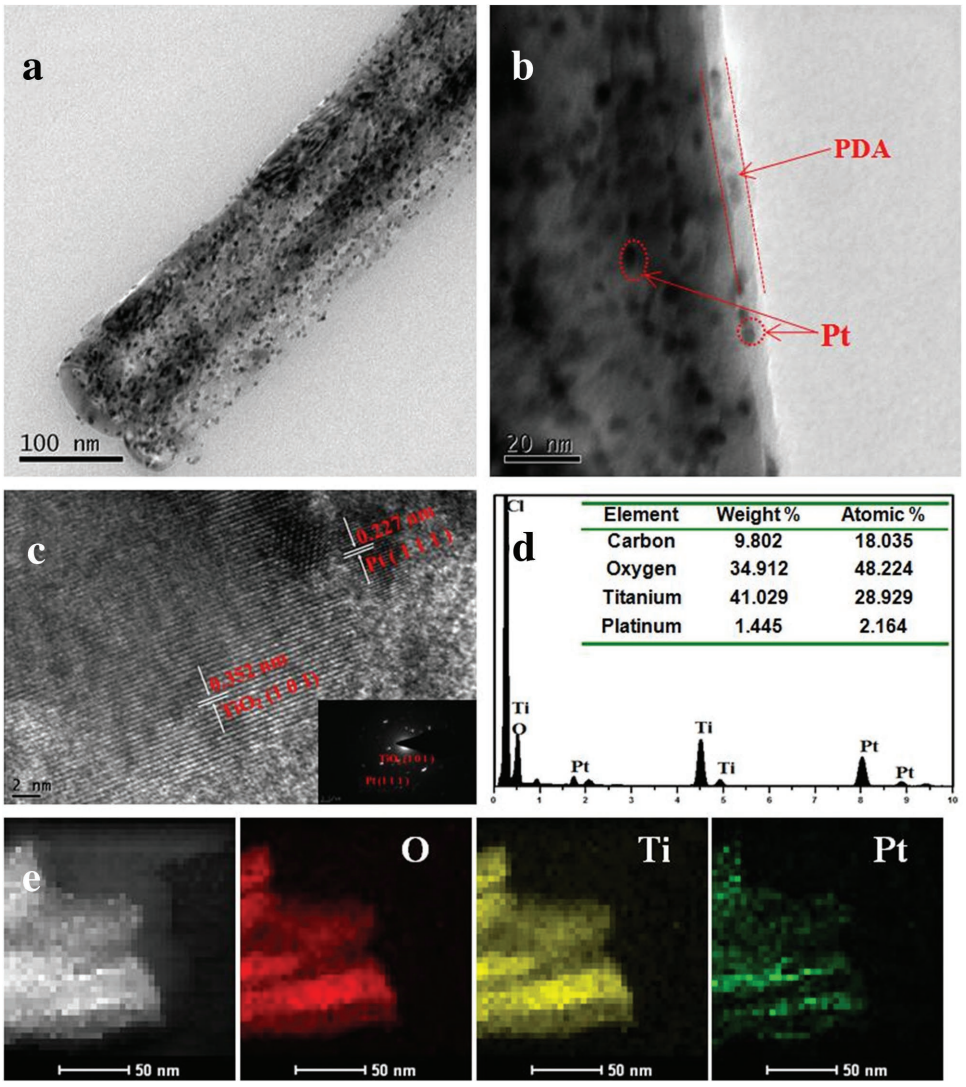

Figure 4. a,b) TEM images of single EPD-reduced Pt@TiO_2 NTAs using 0.4×10^{-3} M chloroplatinic acid solution. c) HRTEM and SAED pattern (inset) of the selected area marked in (b). d) EDX spectrum of the Pt@TiO_2 NTAs. e) EDX mapping of several Pt@TiO_2 NTAs.

decreased when off, thus supporting an immediate photoresponse. Under light irradiation, the pristine TiO_2 NTAs exhibited a photocurrent of 0.003 mA cm^{-2} at an applied potential of 0.26 V. This is attributed to the blocked electron transfer due to the broad band gap and rapid electron–hole recombination. Pt@TiO_2 NTA photoelectrodes are expected to enable an increased photocurrent density under light. The photocurrent density of different Pt@TiO_2 NTA formulations, denoted Pt@TiO_2 NTAs-0.1, 0.2, 0.4, and 0.8 (based on the precursor concentration), were 0.038, 0.046, 0.068, and 0.054 mA cm^{-2}, respectively. These values correspond to 13–23 times the photocurrent density of pristine TiO_2 NTAs. The enhanced photocurrent is attributed to the Pt NPs on the TiO_2 NTAs which increase the charge carrier separation efficiency and suppress the recombination of the electron–hole pairs. The results are in good agreement with the UV-DRS. Pt@TiO_2 NTA-0.4, which possessed the highest photocurrent density, was chosen for the following experiments.

The electrochemical performance of the Pt@TiO_2 NTA-0.4 and pristine TiO_2 NTAs are mainly characterized by electrochemical impedance spectroscopy (EIS) and CV techniques to scrutinize the interfacial properties between electrodes. The diameter of the semicircular curves is directly proportional to the charge transfer resistance (R_{ct}) which estimates the electron transfer kinetics of the redox materials at the electrode surface. As shown in Figure 5c, the Nyquist curve of pristine TiO_2 NTAs essentially forms a straight line, which is characteristic of limited diffusion in electrochemical processes. However, when the electrode is exposed to visible light, the diameter of the semicircle becomes smaller, indicating a higher conductivity. For the as-prepared Pt@TiO_2 NTA-0.4 electrode, the impedance spectrum is composed of two parts: the semicircular part represents R_{ct} at high frequencies and the short linear spike represents the diffusion limited process at lower frequencies. These measurements support that Pt NP decorated TiO_2 NTAs considerably accelerate the movement of electrons by reducing the recombination of electron–hole pairs. The Pt@TiO_2 NTA-0.4 displayed the smallest semicircle diameters, implying the lowest R_{ct}. This property may provide a promising sensing platform for

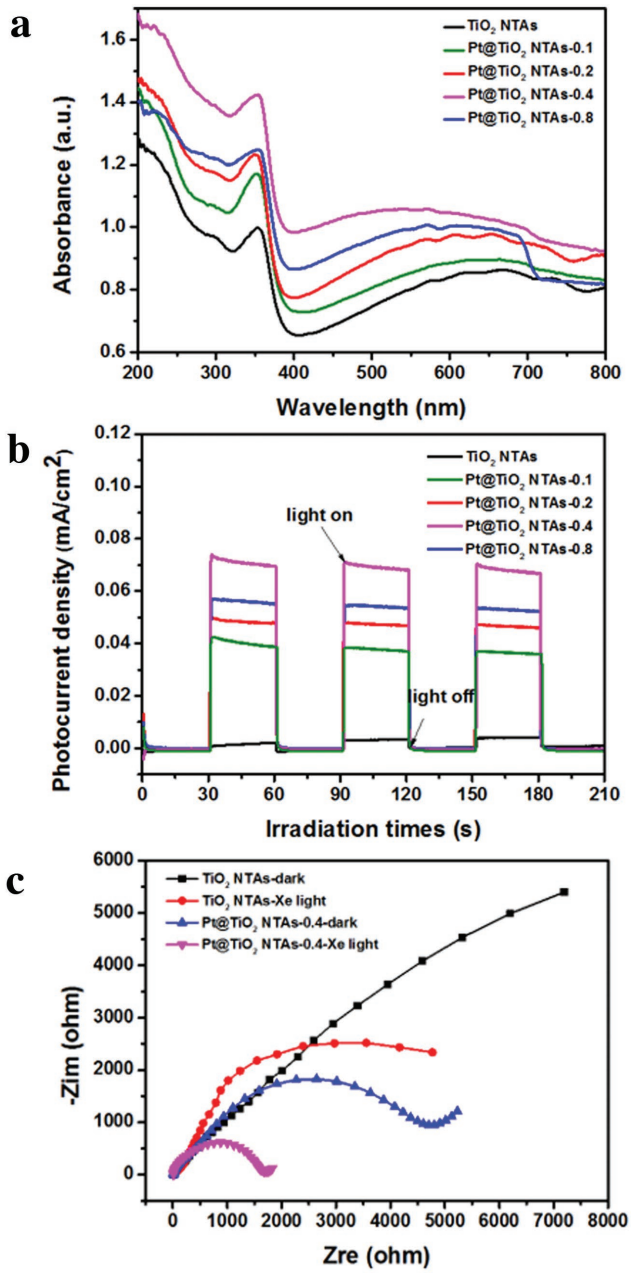

Figure 5. a) UV-DRS absorption spectra of TiO_2 NTAs and EPD-reduced Pt@TiO_2 NTAs with different concentrations of chloroplatinic acid precursor solution. b) Photocurrent responses of pristine TiO_2 NTAs and EPD-reduced Pt@TiO_2 NTAs with concentrations of 0.1×10^{-3}, 0.2×10^{-3}, 0.4×10^{-3}, and 0.8×10^{-3} M chloroplatinic acid precursor solution. c) Nyquist plots of the EIS of pristine TiO_2 NTAs and Pt@TiO_2 NTAs modified by EPD with 0.4×10^{-3} M chloroplatinic acid precursor solution in both dark and illuminated conditions, respectively.

nonenzymatic glucose detection. While Pt@TiO_2 NTA-0.4 electrode performs the lowest R_{ct}, the EIS of others are also shown in Figure S9 (Supporting Information).

2.3. SERS Performance of Pt@TiO_2 NTAs

As shown in **Figure 6**a, the SERS properties of different formulations of EPD-reduced Pt@TiO_2 NTAs were evaluated by detecting the SERS spectra of R6G. All samples were washed with deionized water after being immersed in the R6G for 1 h in dark. The SERS intensity of R6G adsorbed on the TiO_2 NTAs with Pt seeds are significantly enhanced. No Raman spectra are detected for R6G in the absence of Pt NPs. Based on the reported values,[44] one strong peak at 144 cm^{-1} and three weak peaks at 396, 515, and 637 cm^{-1} can be attributed to the O–Ti–O bending of anatase. The bands at 614 and 774 cm^{-1} can be assigned to the C–C–C in-plane vibration mode and C–H out-of-plane bend mode, respectively. The bands at 1311 and 1575 cm^{-1} are assigned to the N–H in-plane bend modes, and 1184, 1362, 1509, and 1649 cm^{-1} are assigned to the C–C stretching modes of R6G. The SERS intensities sharply increase with increasing amounts of Pt NP on the TiO_2 NTAs. SERS spectra of 10^{-4} M R6G on pristine TiO_2 NTAs and EPD-reduced Pt@TiO_2 NTAs with different cycles (5, 10, 20, 40 cycles) of CV technique during the electropolymerization of dopamine on TiO_2 NTAs are shown in Figure S10a (Supporting Information) and the Pt@TiO_2 NTA-20 electrode shows the highest intensity of R6G. Figure 6b shows the intensities of SERS spectra of R6G at concentrations from 10^{-4} to 10^{-9} M. The peaks at 1649 cm^{-1} decrease in intensity with the decreased concentration of R6G. Despite this, the peak is clearly observable at concentrations as low as 10^{-8} M.

The enhancement factor (EF) for the samples was estimated according to the following equation:[45]

$$\mathrm{EF} = \frac{I_{\mathrm{SERS}}\, C_0}{I_0\, C_{\mathrm{SERS}}} \tag{1}$$

where C_{SERS} and I_{SERS} are the concentration of R6G and the corresponding peak intensity at 1649 cm^{-1} under SERS conditions, respectively. While, C_0 and I_0 are the respective concentration of R6G and the corresponding peak intensity at 1649 cm^{-1} in the absence of SERS conditions (Figure S10b, Supporting Information). The EF was calculated to be 4.3×10^4 for EPD-reduced Pt@TiO_2 NTA-0.4. We believe the local electromagnetic field enhancement induced by the excitation of the surface plasmons is the major mechanism for SERS.[46] The electric field increases significantly on top of the Pt NPs and in-between them. This is attributed to the strong near-field couple between the Pt NPs and localized surface plasmon resonance effect which result in enhancement of the Raman intensity of R6G molecules adsorbed on the surface.[47] In addition, charge transfer between the Pt NPs and TiO_2 NTAs can enhance the SERS effects under laser irradiation in which some vibrational modes are more strongly excited.

Photocatalytic degradation of R6G by TiO_2 has been studied. A typical UV-assisted self-cleaning measurement was carried out under UV irradiation for a certain time with the decreasing intensity of the characteristic Raman signal, indicating the degradation of surface adsorbed R6G. Figure 6c gives the relative spectral intensities of the degrading R6G as a function of UV irradiation time. After 30 min of UV irradiation, the intensity of R6G signals sharply decreased and nearly vanished after 150 min of UV irradiation. This indicates that the substrate indeed preserved photocatalytic

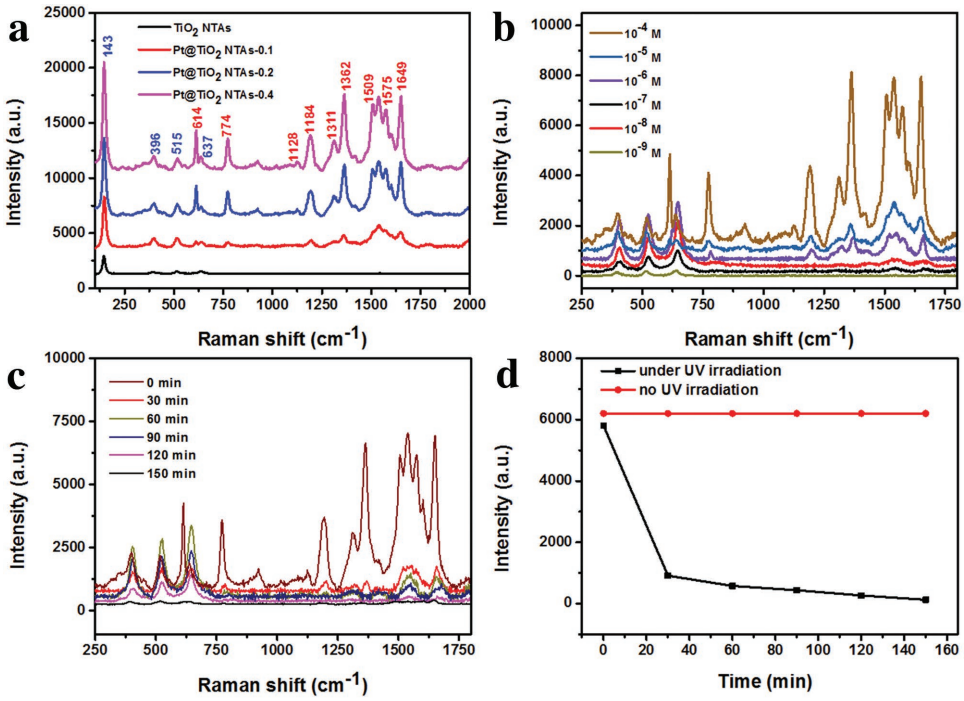

Figure 6. a) SERS spectra of 10^{-4} M R6G on pristine TiO_2 NTAs and EPD-reduced Pt@TiO_2 NTAs with different concentrations of chloroplatinic acid precursor solution (0.1×10^{-3}, 0.2×10^{-3}, 0.4×10^{-3} M). b) SERS spectra for Pt@TiO_2 NTA-0.4 probed with various R6G concentrations from 10^{-4} M to 10^{-9} M. c) Raman spectra of R6G on Pt@TiO_2 NTA-0.4 under UV irradiation from 0 to 150 min at time intervals of 30 min. d) Plot of the SERS intensities at 1649 cm^{-1} versus the time with and without UV irradiation.

functionality. The SERS peak intensity at 1649 cm^{-1} displays the concentration of 10^{-4} M R6G and can be utilized to evaluate the self-cleaning ability of Pt@TiO_2 NTA sample, and it can be seen that the five times recycled Pt@TiO_2 NTA-0.4 does not conspicuously affect its SERS and self-cleaning ability (Figure S11, Supporting Information). The SERS intensities at 1649 cm^{-1} are monitored and the curve is fitted with the UV irradiation time (Figure 6d). The general photocatalytic reaction of R6G is as follows:[48]

$$C_{28}H_{32}N_2O_3 + O_2 \xrightarrow{Pt/TiO_2, hv} CO_2 + H_2O + HNO_3 + (\text{small molecules}) \quad (2)$$

Generally, the photodegradation reaction of R6G can be described by the Langmuir–Hinshelwood mechanism:

$$\ln\left(\frac{C}{C_0}\right) = kt \quad (3)$$

Therefore, the photocatalytic activity can be quantitatively estimated by the evaluation of k, where k is apparent-reaction-rate constant, C_0 is initial concentration of R6G, and C is the concentration of R6G after periods of degradation.

2.4. Photo-Electrocatalysis and Amperometric Determination of Glucose at Pt@TiO_2 NTAs

For evaluating the photoelectrocatalytic activity of the as-prepared Pt@TiO_2 NTAs, CV measurements were carried out with different concentrations of glucose to investigate the electrocatalytic oxidization behavior of pristine TiO_2 NTAs and EPD-reduced Pt@TiO_2 NTA-0.4 under visible light (**Figure 7**b). Three well-defined anodic current responses can be directly observed. The peak potential at –8.5 V can be attributed to hydrogen desorption. The catalytic oxidation of glucose to gluconic acid and the generation of H_2O_2 occurred at around +0.2 V (reaction 4). A pair of redox peaks is shown in the range of –5.0 to –4.0 V, which correspond to the reduction and oxidization of H_2O_2 conducted on the cathode and anode, respectively (reactions 5 and 6).[49] Additionally, enhancements of the anodic current create a corresponding of any increase in the concentration of glucose. In comparison, the redox response to glucose at different concentrations was poorly measured on the TiO_2 NTAs (Figure 7c), indicating the importance of the Pt NPs deposited by EPD on the TiO_2 NTAs (Figure 7a). As shown in Figure S12 (Supporting Information), the color of the electrolyte changed from transparent to yellow after the electrocatalytic oxidization. This supports the transformation of glucose to gluconic acid:

$$\text{Glucose} + O_2 \xrightarrow{PtNPs} \text{Gluconic acid} + H_2O_2 \quad (4)$$

$$H_2O_2 + 2H^+ + 2e^- \xrightarrow{electrode} 2H_2O \ (\text{cathodic response}) \quad (5)$$

$$H_2O_2 \xrightarrow{electrode} O_2 + 2H^+ + 2e^- \ (\text{anodic response}) \quad (6)$$

The amperometric response of pristine TiO_2 NTAs and EPD-reduced Pt@TiO_2 NTA electrodes to glucose with different concentrations were investigated (**Figure 8**a). Samples were subjected to constant stirring (250 rpm) at 25 s intervals between glucose injections in 0.1 M NaOH at an applied potential of –0.4 V. It can be seen that the pristine TiO_2 NTA

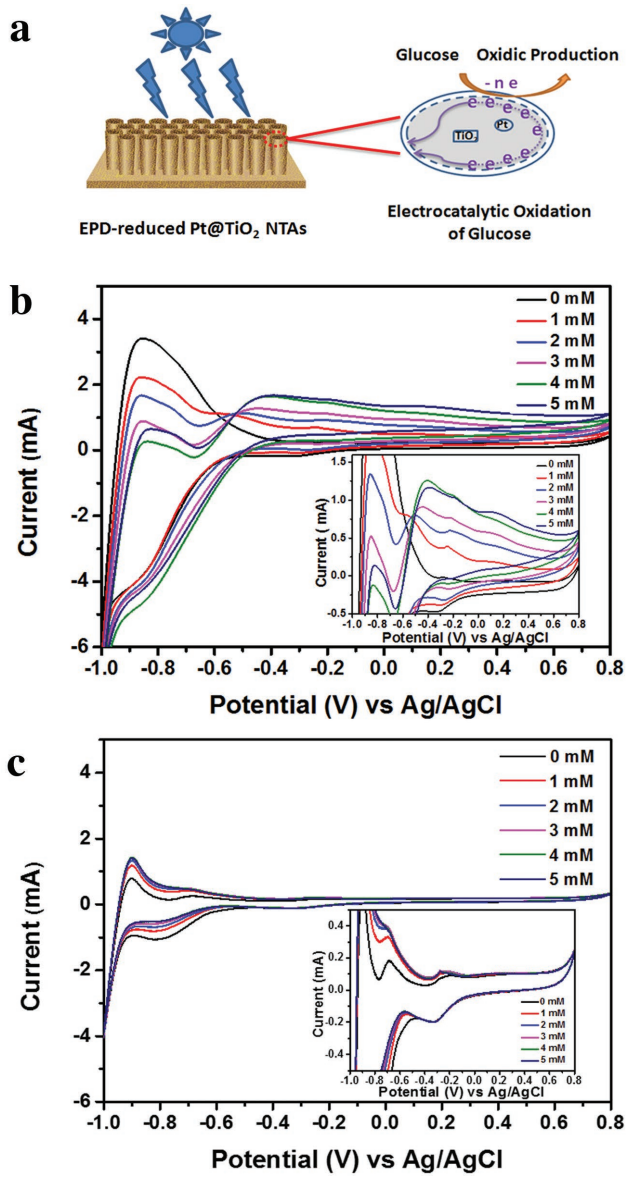

Figure 7. a) A schematic illustration of electron transfer through the Pt@TiO_2 NTA interface during the photo-electrocatalytic oxidation of glucose. CVs of b) the Pt@TiO_2 NTA-0.4 electrode and c) the pristine TiO_2 NTA electrode in 0.1 M NaOH containing different concentrations of glucose at a scan rate of 50 mV s^{-1}.

presents no obvious current response to successive injections of glucose ranging from 0.1×10^{-3} to 4.5×10^{-3} M. Whereas, for Pt@TiO_2 NTA-0.4 electrode, a well-defined step-wise current increase was observed with changes in glucose concentration. In the inset of Figure 8a, the electrode performs in an approximately linear fashion with a correlation coefficient of 0.996 and a sensitivity of 0.056 mA mM^{-1} cm^{-2} (calculated with 0.25 mA m M^{-1} and an area of 4.5 cm^2). The detection limit was found to be 0.02×10^{-3} M at a signal-to-noise ratio of 3 for the as-prepared Pt@TiO_2 NTA electrodes. The high sensitivity may be attributed to the Pt NPs which provide large specific surface areas and show excellent photo-electrocatalytic performance. One problem with many nonenzymatic sensors is the interference of other organic molecules in the blood, such as AA and UA, which can be oxidized at similar potential as glucose. We studied the influence of AA and UA (0.1×10^{-3} M) on the oxidation and sensitivity of glucose by EPD-reduced Pt@TiO_2 NTA electrodes. As shown in Figure 8b, well-defined current responses to glucose are obtained. Only a very slight current response to AA and UA was registered by the sensor. These results substantiated the electrodes' sensitivity to glucose detection even in the presence of chemical interference.

Additionally, the long-term stability of the electrodes was evaluated by CV (1×10^{-3} M glucose solution in 0.1 M NaOH). After daily measurement, the electrodes were dried after washing and stored under ambient conditions. After two weeks, the current intensity of the redox peaks of glucose exhibited only a slight decrease (Figure S13, Supporting Information). Clearly, the self-cleaning ability of the modified electrodes is the other distinguishing feature. Successive amperometric measurements were carried out on a Pt@TiO_2 NTA electrode. A 0.5% relative standard deviation was observed between current values that the electrode was unaffected by the presence of gluconic acid and H_2O_2 as well as demonstrating a high reusability. This phenomenon is attributed to the strong adhesive force of the PDA film to both the TiO_2 NTAs and the Pt NPs.

3. Conclusion

In summary, we have successfully developed a mussel-inspired, fast, and cost-effective strategy for electrochemically induced polymerization of dopamine under mild acid conditions. This strategy renders the creation of uniform Pt NP-anchored vertically aligned TiO_2 nanotube array composites (i.e., Pt@TiO_2 NTA). These as-prepared Pt@TiO_2 NTA electrodes substantially enhanced the surface-enhanced Raman scattering sensitivity of rhodamine 6G, and improved the photo-electrochemical performance of the arrays at a low overpotential to produce effective electrochemical biosensors for glucose detection. The resulting sensors possessed enhanced sensitivity and selectivity as well as long-term stability and self-cleaning abilities. Mussel-inspired PDA is a well-known material. However, the use of this material system to craft a new class of low-cost, simple, and selective sensing materials with the potential for easy generalization represents an important development for the field of materials science and green technology.

4. Experimental Section

Preparation of Two-Step Anodized TiO_2 NTAs: The self-organized TiO_2 NTAs were produced through a two-step anodization in a traditional two-electrode system with Ti foil (purity >99.7%, 0.127 mm in thickness, Aldrich) as the anode and Pt foil (purity > 99.9%) as the cathode, and a potentiostat was used to drive the anodization. Prior to anodization, the titanium foil (3.0 cm × 1.5 cm) was degreased by sonicating in 1 M H_2SO_4, acetone, and ethanol followed by rinsing with distilled water for 20 min. In the first step, anodization was carried out in an ethylene glycol electrolyte containing 0.5 wt% NH_4F (>98%) and 2 vol% H_2O. The applied potential and oxidation time were 55 V and 2 h, respectively. After being ultrasonically cleaned in distilled

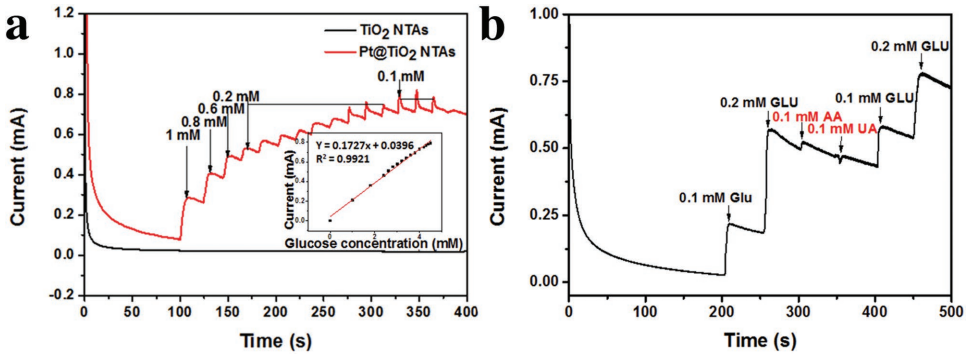

Figure 8. a) Amperometric response of pristine TiO_2 NTAs and EPD-reduced Pt@TiO_2 NTA-0.4 electrodes to successive injections of various glucose concentrations under constant stirring at 25 s intervals in 0.1 M NaOH at –0.4 V. Inset: the linear relationship between the catalytic current and the glucose concentration. b) Amperometric response of Pt@TiO_2 NTA-0.4 electrode to glucose at different concentrations in the absence and presence of 0.1×10^{-3} M AA and UA in 0.1 M NaOH at an applied potential of –0.4 V.

water, the resulting TiO_2 film was removed from the Ti foils. Subsequently, the cleaned Ti foil was reanodized at 55 V for 6 min to complete the second anodization. Finally, after being rinsed with distilled water and dried in air, the as-prepared TiO_2 NTAs were annealed at 450 °C for 2 h with a heating and cooling rate of 5 °C min^{-1} in high purity N_2 for improved crystallinity.

Synthesis of PDA-Modified TiO_2 NTAs: Biomimetic PDA films were deposited onto the inner and outer surfaces of TiO_2 NTAs by EPD. Saturated calomel electrode, platinum plate, and the as-prepared anodized TiO_2 NTAs were used as the reference electrode, counter electrode, and working electrode, respectively. First, aqueous dopamine solution (2 mg mL^{-1}) was prepared by dissolving oxytyramine hydrochloride (98%) in the Tris-HCl buffer (50 mL, 1 mg mL^{-1}, pH = 7.4) with ultrasonication for 5 min. CV was employed to prepare PDA coatings under a 500 W Xenon lamp with a UV light cutoff filter (λ nder a 500 serving as the visible light source. EPD was then carried out by consecutive CV sweeps in the potential range from –1 to 1 V at a rate of 0.2 V s^{-1} for different cycles under inert nitrogen atmosphere. The thickness of PDA films on TiO_2 NTAs can be controlled by adjusting the number of cycles. Finally, the resulting PDA-modified TiO_2 NTAs were washed with deionized water to remove residues and dried under 80 °C for 1 h.

Assembly of EPD-Reduced Pt@TiO_2 NTAs: Pt NPs were attached to the surface of the PDA-modified TiO_2 NTAs by an in situ reductive reaction due to the numerous functional groups (—OH, —NH_2) on the surface of PDA. Briefly, the PDA-coated TiO_2 NTAs were submerged in various concentrations of chloroplatinic acid solution (0.1×10^{-3}–0.8×10^{-3} M) around 50 mL, and the system was magnetically stirred at a speed of 200 rpm under 90 °C for 3 h. After ultrasonication, the electrodes were rinsed with distilled water three times to remove residual ions and baked at 80 °C for 1 h. Finally, the Pt@TiO_2 NTA combination electrodes were formed through the in situ EPD reduction process. Depending on the different concentrations of Pt^{4+} ions, sample electrodes were marked as Pt@TiO_2 NTA-0.1 to Pt@TiO_2 NTA-0.8. The typical procedure for the Pt@TiO_2 NTAs is very straightforward and illustrated in **Scheme 1**.

Characterization of the Pt@TiO_2 NTAs: The structure and morphology of the Pt@TiO_2 NTAs modified by PDA were investigated

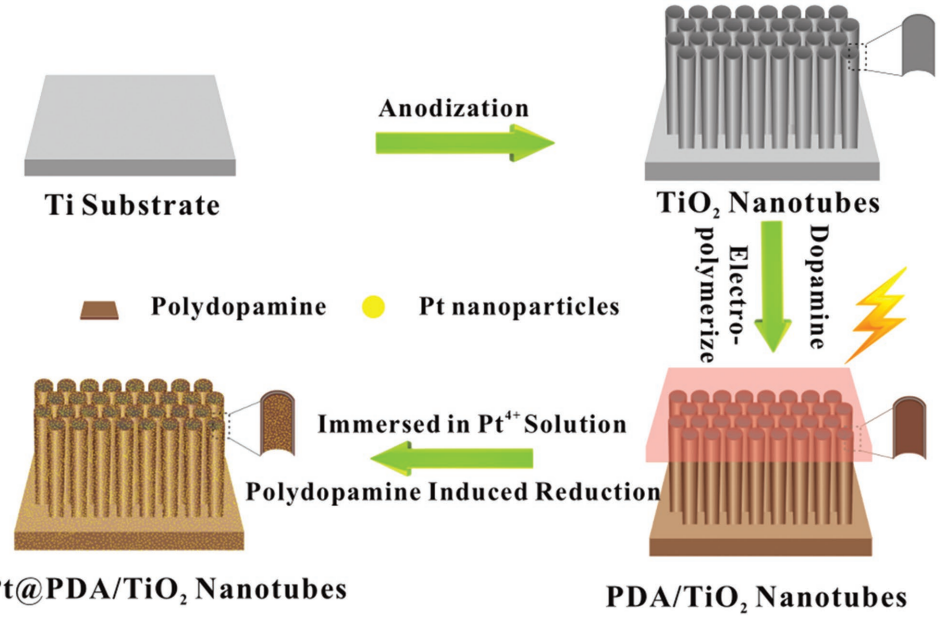

Scheme 1. Schematic illustration of the preparation of EPD-reduced Pt@TiO_2 NTAs.

by field emission scanning electron microscopy (Hitachi S-4800) at 3.0 kV. The microstructure, composition, and presence of Pt were further confirmed by using a TEM (FEI TecnaiG-20 operated at 200 kV). An energy dispersive X-ray spectrometer fitted to the TEM was applied for elemental analysis. The chemical components were verified by a Kratos Axis-Ultra XPS with a 100 W Al-Kα X-ray source. The binding energies were normalized to the signal for C 1s at 284.5 eV. The crystal phases were identified by using X-ray diffraction with Cu-Kα radiation (Philips, X'pert-Pro MRD). UV-DRS was recorded in the range of 250–800 nm at room temperature using a UV-3600.

SERS Spectra Measurement: A Raman spectrometer (HOKIBA JOBIN YVON, FM4P-TCSPC) with an air–argon ion laser as the excitation source (λ_{ex} = 532 nm) was used to carry out all the measurements. All substrates were rinsed with deionized water after immersion in the appropriate precursor solutions for 1 h. In order to reduce the catalytic and photochemical decomposition caused by laser exposure, the laser beam was focused to a size of 2 μm with a low power of 0.5 mW, and an accumulation time of 5 s. For reducing error propagation among the measurements, the average of three SERS spectra at different positions on the substrate was taken.

Photo-Electrochemical Testing: The electrochemical performance of Pt@TiO_2 NTA electrodes were investigated by CV measurements, chronoamperometry, and EIS. All electrochemical experiments were performed in a standard three-electrode system utilizing a PGSTAT302N electrochemical workstation (AUTOLAB, Switzerland). Before all electrochemical measurements, all of the as-prepared electrodes were immersed in phosphate buffer saline (PBS) (pH = 7.2) for 15 min to remove the contaminants. Photocurrent response EIS measurements were carried out in a standard three-electrode configuration with the TiO_2 NTAs or EPD-reduced Pt@TiO_2 NTAs as the working electrodes with a Pt wire as the reference electrode, Ag/AgCl as the reference electrode in 0.1 M Na_2SO_4 aqueous electrolyte solution (pH = 7.0). The working electrodes were irradiated by a GY-10 Xenon lamp and with an irradiation separation distance of 15 cm. The focused incident light intensity on the flask was ≈100 mW cm^{-2}. The EIS measurements were performed in both dark and illuminated states at open circuit voltages over a frequency range from 10^5 to 10^{-2} Hz with a potential amplitude of 5 mV to characterize the interfacial properties of the electrodes. The volume of the electrolyte was 50 mL consisting 0.1 mol L^{-1} NaOH with and without different concentrations of glucose. AA and UA were added during the interference testing of glucose.

Supporting Information

Supporting Information is available from the Wiley Online Library or from the author.

Acknowledgements

The authors thank the National Natural Science Foundation of China (51502185 and 21501127), the Natural Science Foundation of Jiangsu Province of China (BK20140400). The authors also acknowledge the funds from the Priority Academic Program Development of Jiangsu Higher Education Institutions (PAPD), and the Project for Jiangsu Scientific and Technological Innovation Team (2013).

[1] a) A. Fujishima, K. Honda, *Nature* **1972**, *238*, 37; b) R. Asahi, T. Morikawa, T. Ohwaki, K. Aoki, Y. Taga, *Science* **2001**, *293*, 269; c) K. Nakata, A. Fujishima, *J. Photochem. Photobiol.* **2012**, *3*, 169.

[2] a) K. Li, A. Mazare, P. Schmuki, *Chem. Rev.* **2014**, *114*, 9385; b) F. X. Xiao, S. F. Hung, J. W. Miao, H. Y. Wang, H. B. Yang, B. Liu, *Small* **2015**, *11*, 554; c) P. Roy, S. Berger, P. Schmuki, *Angew. Chem. Int. Ed.* **2011**, *50*, 2904.

[3] a) J. Y. Huang, Y. K. Lai, F. Pan, L. Yang, H. Wang, K. Q. Zhang, H. Fuchs, L. F. Chi, *Small* **2014**, *10*, 4865; b) Y. K. Lai, F. Pan, C. Xu, H. Fuchs, L. F. Chi, *Adv. Mater.* **2013**, *25*, 1682; c) S. N. Zhang, J. Y. Huang, Y. X. Tang, S. H. Li, M. Z. Ge, Z. Chen, K. Q. Zhang, Y. K. Lai, *Small* **2017**, *13*, 1600687.

[4] a) Y. H. Hu, *Angew. Chem. Int. Ed.* **2012**, *51*, 12410; b) Y. Hou, X. Y. Li, Q. D. Zhao, X. Quan, G. H. Chen, *Adv. Funct. Mater.* **2010**, *20*, 2165; c) C. K. Xu, P. H. Shin, L. L. Cao, J. M. Wu, D. Gao, *Chem. Mater.* **2010**, *22*, 143.

[5] a) K. S. Liu, M. Y. Cao, A. Fujishima, L. Jiang, *Chem. Rev.* **2014**, *114*, 10044; b) Y. Liu, Q. Yao, X. Wu, T. Chen, Y. Ma, C. N. Ong, J. Xie, *Nanoscale* **2016**, *8*, 10145; c) Y. Y. Zhang, B. Wu, Y. X. Tang, D. Q. Qi, N. Wang, X. T. Wang, X. L. Ma, T. C. Sum, X. D. Chen, *Small* **2016**, *12*, 2291.

[6] a) M. D. Ye, J. J. Gong, Y. K. Lai, C. J. Lin, Z. Q. Lin, *J. Am. Chem. Soc.* **2012**, *134*, 15720; b) M. Y. Wang, D. J. Zheng, M. D. Ye, C. C. Zhang, B. B. Xu, C. J. Lin, L. Sun, Z. Q. Lin, *Small* **2015**, *11*, 1436; c) G. H. Chen, S. Z. Ji, Y. H. Sang, S. J. Chang, Y. N. Wang, P. Hao, J. Claverie, H. Liu, G. W. Yu, *Nanoscale* **2015**, *7*, 3117.

[7] a) Y. Q. Yang, G. Liu, J. T. S. Irvine, H. M. Cheng, *Adv. Mater.* **2016**, *28*, 5850; b) L. X. Zheng, S. C. Han, H. Liu, P. P. Yu, X. S. Fang, *Small* **2016**, *12*, 1527; c) Y. Zhang, Z. Jiang, J. Huang, L. Y. Lim, W. Li, J. Deng, D. Gong, Y. Tang, Y. Lai, Z. Chen, *RSC Adv.* **2015**, *5*, 79479.

[8] a) W. Zhou, W. Li, J. Q. Wang, Y. Qu, Y. Yang, Y. Xie, K. F. Zhang, L. Wang, H. G. Fu, D. Y. Zhao, *J. Am. Chem. Soc.* **2014**, *136*, 9280; b) Y. Lai, L. X. Lin, F. Pan, J. Huang, R. Song, Y. Huang, C. Lin, H. Fuchs, L. Chi, *Small* **2013**, *9*, 2945; c) X. Yu, L. Wang, J. Zhang, W. Guo, Z. Zhao, Y. Qin, X. Mou, A. Li, H. Liu, *J. Mater. Chem. A* **2015**, *3*, 19129.

[9] a) Y. X. Tang, Y. Y. Zhang, X. H. Rui, D. P. Qi, Y. F. Luo, W. R. Leow, S. Chen, J. Guo, J. Wei, W. L. Li, J. Y. Deng, Y. K. Lai, B. Ma, X. D. Chen, *Adv. Mater.* **2016**, *28*, 1567; b) M. Y. Wang, M. D. Ye, J. Iocozzia, C. J. Lin, Z. Q. Lin, *Adv. Sci.* **2016**, *3*, 1600024; c) M. Z. Ge, C. Y. Cao, S. H. Li, Y. X. Tang, L. N. Wang, N. Qi, J. Y. Huanag, K. Q. Zhang, S. S. Al-Deyab, Y. K. Lai, *Nanoscale* **2016**, *8*, 5226.

[10] a) Y. K. Lai, J. Y. Huang, Z. Q. Cui, M. Z. Ge, K. Q. Zhang, Z. Chen, L. F. Chi, *Small* **2016**, *12*, 2203; b) Z. M. Ge, C. Y. Cao, J. Y. Huang, S. H. Li, S. N. Zhang, S. Deng, Q. S. Li, K. Q. Zhang, Y. K. Lai, *Nanotechnol. Rev.* **2016**, *5*, 75; c) M. Y. Wang, J. Ioccozia, L. Sun, C. J. Lin, Z. Q. Lin, *Energy Environ. Sci.* **2014**, *7*, 2182.

[11] a) J. M. Choi, S. Song, M. T. Hörantner, H. J. Snaithand, T. Park, *ACS Nano* **2016**, *10*, 6029; b) M. Z. Ge, C. Y. Cao, J. Y. Huang, S. H. Li, Z. Chen, K. Q. Zhang, S. S. Al-Deyab, Y. K. Lai, *J. Mater. Chem. A* **2016**, *4*, 6772; c) M. Z. Ge, Q. S. Li, C. Y. Cao, J. Y. Huang, S. H. Li, S. N. Zhang, Z. Chen, K. Q. Zhang, S. S. Al-Deyab, Y. K. Lai, *Adv. Sci.* **2017**, *4*, 1600152.

[12] Q. Yang, M. Long, L. Tan, Y. Zhang, J. Ouyang, P. Liu, A. D. Tang, *ACS Appl. Mater. Interfaces* **2015**, *7*, 12719.

[13] M. H. Ryou, Y. M. Lee, J. K. Park, J. W. Choi, *Adv. Mater.* **2011**, *23*, 3066.

[14] H. Lee, S. M. Dellatore, W. M. Miller, P. B. Messersmith, *Science* **2007**, *318*, 426.
[15] M. A. P. Bloomfield, A. H. Ashok, N. H. Volkow, O. D. Howes, *Science* **2016**, *539*, 369.
[16] M. Krogsgaard, M. A. Behrens, J. S. Pedersen, H. Birkedal, *Biomacromolecules* **2013**, *14*, 297.
[17] Z. Zhang, J. Zhang, B. Zhang, J. Tang, *Nanoscale* **2013**, *5*, 118.
[18] Y. Xie, B. Yan, H. Xu, J. Chen, Q. Liu, Y. Deng, H. Zeng, *ACS Appl. Mater. Interfaces* **2014**, *6*, 8845.
[19] a) M. H. Ryou, D. J. Lee, J. N. Lee, Y. M. Lee, J. K. Park, J. W. Choi, *Adv. Energy Mater.* **2012**, *2*, 645; b) W. X. Mao, X. J. Lin, W. Zhang, Z. X. Chi, R. W. Lyu, A. M. Cao, L. J. Wan, *Chem. Commun.* **2016**, *52*, 7122.
[20] C. D. Fiorillo, *Science* **2013**, *341*, 546.
[21] Y. Cong, T. Xia, M. Zou, Z. Li, B. Peng, D. Guo, Z. Deng, *J. Mater. Chem. B* **2014**, *2*, 3450.
[22] H. Wei, N. Insin, J. Lee, H. S. Han, M. C. Cordero, W. H. Liu, M. G. Bawendi, *Nano Lett.* **2012**, *12*, 22.
[23] A. Ma, Y. Xie, J. Xu, H. Zeng, H. Xu, *Chem. Commun.* **2015**, *51*, 1469.
[24] S. Nie, S. R. Emory, *Science* **1997**, *275*, 1102.
[25] M. Kalbac, H. Farhat, J. Kong, P. Janda, L. Kavan, *Nano Lett.* **2011**, *11*, 1957.
[26] a) S. C. Xu, B. Y. Man, S. Z. Jiang, J. H. Wang, J. Wei, S. D. Xu, H. P. Liu, S. B. Gao, H. L. Liu, Z. H. Li, H. S. Li, H. W. Qiu, *ACS Appl. Mater. Interfaces* **2015**, *7*, 10977; b) Y. Lee, T. G. Park, *Langmuir* **2011**, *27*, 1965.
[27] S. M. Morton, L. Jensen, *J. Am. Chem. Soc.* **2009**, *131*, 4090.
[28] M. H. Asif, S. M. Usman Ali, O. Nur, M. Willander, C. Brännmark, P. Stralfors, U. H. Englund, F. Elinder, B. Danielsson, *Biosens. Bioelectron.* **2010**, *25*, 2205.
[29] S. J. Updike, G. P. Hicks, *Nature* **1967**, *214*, 986.
[30] D. Y. Zhai, B. Liu, Y. Shi, L. J. Pan, Y. Q. Wang, W. B. Li, R. Zhang, G. H. Yu, *ACS Nano* **2013**, *7*, 3540.
[31] M. Long, L. Tan, H. T. Liu, Z. He, A. D. Tang, *Biosens. Bioelectron.* **2014**, *59*, 243.
[32] H. J. Choi, S. M. Jung, J. M. Seo, D. W. Chang, L. Dai, *Nano Energy* **2012**, *1*, 534.
[33] R. A. Blaik, E. Lan, Y. Huang, B. Dunn, *ACS Nano* **2016**, *10*, 324.
[34] a) Y. Zhao, Y. W. Yeh, R. Liu, J. M. You, F. L. Qu, *Solid State Sci.* **2015**, *45*, 9; b) Y. H. Ding, L. T. Weng, M. Yang, Z. L. Yang, X. Lu, N. Huang, Y. Leng, *Langmuir* **2014**, *30*, 12258.
[35] a) X. Du, L. Li, J. Li, C. Yang, N. Frenkel, A. Welle, S. Heissler, A. Nefedov, M. Grunze, P. A. Levkin, *Adv. Mater.* **2014**, *26*, 8029; b) V. Ball, J. Gracio, M. Vila, M. K. Singh, M. H. Metz-Boutigue, M. Michel, J. Bour, V. Toniazzo, D. Ruch, M. J. Buehler, *Langmuir* **2013**, *29*, 12754; c) K. Kang, S. Lee, R. Kim, I. S. Choi, Y. Nam, *Angew. Chem. Int. Ed.* **2012**, *51*, 13101.
[36] C. Zhang, Y. Ou, W. X. Lei, L. S. Wan, J. Ji, Z. K. Xu, *Angew. Chem. Int. Ed.* **2016**, *55*, 3054.
[37] J. L. Wang, B. C. Li, Z. J. Li, K. F. Re, L. J. Jin, S. M. Zhang, H. Chang, Y. X. Sun, J. Ji, *Biomaterials* **2014**, *35*, *7679*.
[38] Q. Liu, N. Y. Wang, J. Caro, A. S. Huang, *J. Am. Chem. Soc.* **2013**, *135*, 17679.
[39] P. L. Wang, Y. L. Zhou, Y. Wen, F. Wang, H. F. Yang, *RSC Adv.* **2015**, *5*, 36368.
[40] Z. H. Zhao, J. Tian, Y. H. Sang, A. Cabot, H. Liu, *Adv. Mater.* **2015**, *26*, 2557.
[41] W. Kudernatsch, G. W. Peng, H. Zeuthen, Y. H. Bai, L. R. Merte, L. Lammich, F. Besenbacher, M. Mavrikakis, S. Wendt, *ACS Nano* **2015**, *9*, 7804.
[42] B. T. Sneed, A. P. Young, D. Jalalpoor, M. C. Golden, S. J. Mao, Y. Jiang, Y. Wang, C. K. Tsung, *ACS Nano* **2014**, *8*, 7239.
[43] a) S. Dick, M. P. Konrad, W. W. Y. Lee, H. McCabe, J. N. McCracken, T. M. D. Rahman, A. Stewart, Y. K. Xu, S. E. J. Bell, *Adv. Mater.* **2016**, *28*, 5705; b) D. Manchon, J. Lermé, T. P. Zhang, A. Mosset, C. Jamois, C. Bonnet, J. M. Rye, A. Belarouci, M. Broyer, M. Pellarin, E. Cottancin, *Nanoscale* **2015**, *7*, 1181; c) A. Lamberti, A. Virga, A. Chiadò, A. Chiodoni, K. Bejtka, P. Rivolo, F. Giorgis, *J. Mater. Chem. C* **2015**, *3*, 6868.
[44] B. H. Zhang, S. H. Wang, L. H. Lu, K. L. Ai, G. Zhang, X. L. Cheng, *Adv. Funct. Mater.* **2008**, *18*, 2348.
[45] Q. Shao, R. H. Que, M. W. Shao, L. Cheng, S. T. Lee, *Adv. Funct. Mater.* **2012**, *22*, 2067.
[46] J. N. Anker, W. P. Hall, O. Lyandres, N. C. Shah, J. Zhao, R. P. Van Duyne, *Nat. Mater.* **2008**, *7*, 442.
[47] K. Liu, Y. C. Bai, L. Zhang, Z. B. Yang, Q. K. Fan, H. Q. Zheng, Y. D. Yin, C. B. Gao, *Nano Lett.* **2016**, *16*, 3675.
[48] J. W. Zhang, S. A. Winget, Y. R. Wu, D. Su, X. J. Sun, Z. X. Xie, D. Qin, *ACS Nano* **2016**, *10*, 2607.
[49] Y. Huang, J. Cai, Y. Guo, *Appl. Catal., B* **2013**, *129*, 549.

Received: December 23, 2016
Revised: January 27, 2017
Published online: March 10, 2017